Quantitative Understanding of Charge Transfer Mediated Fe^{3+} Sensing and Fast Photoresponse by N-doped Graphene Quantum Dots Decorated on Plasmonic Au Nanoparticles

Ruma Das[a], Hiroshi Sugimoto[b], Minoru Fujii [b], and P. K. Giri[a, c*]

[a]*Department of Physics, Indian Institute of Technology Guwahati, Guwahati -781039, India*

[b] *Department of Electrical and Electronics Engineering, Kobe University, Rokkodai, Nada, Kobe 657, Japan*

[c]*Centre for Nanotechnology, Indian Institute of Technology Guwahati, Guwahati -781039, India*

Abstract: The formation of heterostructure with plasmonic nanoparticles drastically alter the optoelectronic properties of graphene quantum dots (GQDs), resulting in exceptional properties. In the present work, we prepare nitrogen-doped GQDs decorated on gold nanoparticle (Au@N-GQDs) by a one-step green reduction method and study its extraordinary fluorescence and photoresponse characteristics. The as-prepared Au@N-GQDs show more than one order of magnitude enhancement in the fluorescence intensity as compared to the bare N-GQDs, which is attributed to hot electron generation and improved absorption in N-GQDs by local field enhancement and the modification of the edge functional groups. Due to the selective coordination to Fe^{3+} ions, the Au@N-GQDs exhibit extraordinary quenching of fluorescence, with ultrahigh sensitivity for the detection of Fe^{3+} (<1 nM). A new model for the charge transfer dynamics is developed involving the Langmuir's law of adsorption to explain the unusual quenching, which

* Corresponding author, email: giri@iitg.ac.in

strongly deviates from the known models of static/ dynamic quenching. The proposed sensor is successfully implemented for the ultrasensitive detection of Fe^{3+} ions in human serum and Brahmaputra river water samples, representing its high potential applications in clinical as well as environmental diagnosis. Additionally, due to its high absorption in the UV-Vis-NIR region and high charge density with long life excitons, the Au@N-GQDs is utilized as a photodetector with ~10^4 times faster response than that of bare N-GQDs. The Au@N-GQDs based photodetector possesses a high responsivity of ~1.36 A/W and a remarkably high external quantum efficiency of ~292.2 %, which is much superior to the GQDs based photodetectors reported till date. The underlying mechanism of ultrafast photoresponse is ascribed to the transfer of hot electrons along with the tunneling of the electrons from Au NPs to N-GQDs as well as the defect reduction of N-GQDs by the incorporation of Au NPs. Without the use of any charge transporting layer, the outstanding performance of N-GQDs based plasmonic photodetector opens up unique opportunities for future high-speed optoelectronic devices.

Keywords*: N-doped graphene quantum dots; plasmonic hot electrons; nM level Fe^{3+} sensing in human serum; charge transfer dynamic; ultrafast photodetector.*

1. Introduction

The graphitic materials serve as unique structural platforms for the deposition of nanoparticles of noble metals, leading to the formation of functional nanocomposites with improved optical and electrical properties.[1-3] The metal-carbon nanocomposites were extensively studied for catalysis, electrochemical sensing, and other renewable energy-related applications.[2-4] Star et al. detected different toxic gases by metal decorated carbon nanotubes.[5] The detection of

H_2O_2 through the nanocomposite of gold nanoparticles (Au NPs) and nitrogen-doped graphene quantum dots (N-GQDs) by electrochemical method was reported by Ju et al..[3] Recently, Majumder et al. reported reduced graphene oxide (RGO)-wrapped Au nanoplatelets for photocatalytic water splitting as well as electrochemical sensing of H_2O_2 and ascorbic acid.[2] As a catalysts, Au NPs supported on graphene oxide (GO) quantum dots and RGO quantum dots provide higher decomposition of ammonium perchlorate.[6] On the other hand, the enhanced fluorescence quantum yield by the interaction of carbon nanoparticles with Ag, Cu, and Pd nanoparticles was also reported.[1] Majumder et al. also reported the enhancement of the photoluminescence (PL) of RGO by wrapped Au nanoplatelets.[2] Despite the improved optical properties, the applications of metal-carbon nanocomposites have not been exploited much in optoelectronics. In particular, there is no report on N-GQDs decorated Au NPs composites for fluorometric sensing application till date.

Fe^{3+} is one of the essential metal ions in the human body system, and it plays a vital role in cellular metabolism, oxygen transport, enzyme catalysis as well as nucleic acid synthesis processes.[7-9] The dysfunction of Fe^{3+} in the human body can cause several diseases, such as anemia, Parkinson's illness, malaria, Alzheimer's disease, cancer, etc.[9-10] Therefore, effective sensing of Fe^{3+} ion in different food items is highly desirable for healthy living. Considerable research has been devoted to constructing different analysis methods for quantitative and quantitative detection of Fe^{3+}. Earlier, the detection of Fe^{3+} was accomplished by ion-exchange chromatography[11] and spectrophotometric detection using organic dyes.[12] The difficulties in sample preparation and pre-treatment procedures, the requirement of the sophisticated instrumentation and finally the low sensitivity encouraged to find out the alternatives for efficient, rapid and easy sensing of Fe^{3+} ions. Fluorometric methods have been established as time effective,

simple, low cost, selective, and sensitive for the detection of metal ions. Being a fluorescent material, both un-doped and doped GQDs were widely used for the fluorometric sensing applications. Ananthanarayanan et al. used undoped GQDs to sense Fe^{3+} ion down to 7.2 μM,[13] whereas, sulfur-doped GQDs (S-GQD) has been prepared by Li et al. group to detect Fe^{3+} ion down to 4.2 nM.[7] The presence of nitrogen atoms in N-GQDs creates more active sites facilitating efficient interaction with Fe^{3+} and able to sense up to 0.21 nM by the quenching of PL intensity of N-GQDs.[14] Though the sensitivity is not appreciable, different types of functionalization of GQDs were also reported previously for Fe^{3+} sensing.[9, 15]

In the present work, we adopt a simple and green method for the synthesis of Au@N-GQDs without the use of any surfactant. The PL emission of N-GQDs increases significantly by the formation of Au@N-GQDs hetero-structure. By the incorporation of Au NPs, the modification of the functional groups with higher charge density and effective charge separation are observed from detail characterizations. Herein, the as-synthesized Au@N-GQDs is demonstrated as a wide range (1 nM to 10 μM) fluorescence-based sensor for Fe^{3+} ions in human serum and Brahmaputra river water samples with an in-depth study of the quenching mechanism by introducing a new model for charge transfer dynamics.

Despite its fascinating properties, the zero band gap of graphene limits its applications in optoelectronic devices due to low optical absorption, short carrier lifetime, low spectral responsivity, a small difference in dark and light signal.[16-17] Interestingly, GQDs with high surface area, tunable bandgap, high optical absorption, and efficient multiple carrier generation properties extend the potential of graphitic materials in optoelectronics devices.[18-19] Due to the lower carrier density, week conductivity, higher trapping states and defect states, the performance of the GQD based photodetectors could not achieve the desired level of performance needed for commercial

applications. Subsequently, the doped GQDs were introduced to increase the conductivity and carrier density for the higher photocurrent.[20-21] Among them, N-GQDs attract certain attention as a good photodetector due to its n-type conductivity.[21] However, the performance of the GQD based photodetectors has not met the desired level. Lately, due to the adjustable bandgap, strong quantum confinement and ability of electron-hole pair formation, GQDs were implemented in the graphene-based layer staking device as a charge generating layer and significant improvement of the device performance were observed.[22-24] Nguyen et al. recently reported enhanced photoresponsivity of monolayer WSe_2 by the incorporation of N-GQDs as a transporting layer.[25] On the other hand, with a shell of GQDs on Silicon nanowire core, a large photocurrent was achieved due to charge transfer from GQDs.[26] Noteworthy, the performance of graphene-based photodetector has been improved with the aid of surface plasmon effects.[27-29] On the contrary, the improvement of the GQDs based photodetector has been overlooked. In the present work, we demonstrate a major improvement in the performance of the N-GQDs based photodetector by the incorporation of Au NPs by In-situ growth along with the ultrafast photoresponse, and we investigate the underlying mechanism thoroughly. Note that we do not use any charge transporting layer in the N-GQDs based photodetector device reported here.

2. Experimental details

2.1. Material synthesis

At first, the GO was prepared from graphite flakes by using the modified Hummers method[30] and then N-GQDs were synthesized by a solvothermal method with DMF solvent using GO as precursor material. More details are provided in the Supporting Information (SI†), Section S1.[31] Next, the as-synthesized N-GQDs was used as a reducing agent for the preparation of Au NPs decorated with N-GQDs. Note that in the present synthesis, we completely avoided the use of

any surfactant for the reduction of Au NPs as it can affect the surface properties of Au NPs, and thus the interface between the Au NPs and N-GQDs.

For the synthesis of Au@N-GQDs, typically, typically 20 mL of 1 mg/mL as-synthesis N-GQDs solution was heated at 110 °C with stirring for 10 min. Afterward, 2 mL of $HAuCl_4$, 4 H_2O solution (5 mM, 99.9%, Alfa Aesar) was added dropwise into N-GQDs solution, following the method described elsewhere.[31] Immediately, the yellow color of N-GQDs solution started to change to light pink color, indicating the formation of Au@N-GQDs. After the natural cooling to room temperature, Au@N-GQDs was separated by centrifuging the aqueous solution at 13,000 rpm for 10 min. The concentration of the obtained stock solution of Au@N-GQDs was 0.91 mg/mL.

2.2. Detection of Fe^{3+} ions

For the detection of Fe^{3+} ions by Au@N-GQDs, different concentrations of $FeCl_3$ (Merck) stock solutions were prepared with MQ water. Typically, 1 mL of each concentration of $FeCl_3$ was mixed with 0.5 mL of Au@N-GQDs (101 μg/mL) aqueous solution, and consequently, 1 mL of buffer solution (pH 6) was added into the above solution to fix the pH value. The solution was well shaken and kept for 12 min before recording the spectra. In the course of comparison of the sensitivity, the effect of Fe^{3+} with bare N-GQDs (0.5 mL of 120 μg/mL N-GQDs + 1 mL of buffer) and N-GQDs mixed with Au NPs (0.25 mL of 120 μg/mL N-GQDs + 0.25 mL of 20 μg/mL Au NP + 1 mL of buffer) were also considered.

2.3. Device fabrication for photocurrent measurements

In the present case, the Au@N-GQDs Schottky junction photodetector device architecture was adopted with a symmetric structure with two Al electrodes (each of width 1 mm) with a gap of 136 μm for the top contact measurement. At first, a thick uniform layer of Au@N-GQDs was

deposited on 400 nm SiO_2/Si substrate by the repeated spin-coating process followed by heating at 70 °C at each step. Afterward, Al electrodes were deposited through a mask on top of the Au@N-GQDs layer by thermal evaporation at a base pressure of $\sim 1\times10^{-6}$ Torr. For comparison, a similar device was also prepared with bare N-GQDs. Details of characterization and photocurrent measurement procedure are presented in section S2 and S3 (SI†).

3. Results and discussions

3.1. Morphology and structural characterizations

The morphology of the as-grown N-GQD and Au@N-GQDs are studied with TEM and AFM analyses. Figure 1(a) shows the well-dispersed N-GQDs of a circular shape, synthesized by the solvothermal method. The statistical size distribution of the N-GQDs is shown in the inset of Figure 1(a). The average size (diameter) of the N-GQDs is obtained as ~3.6 nm by the lognormal fitting, as shown in the inset of Figure 1(a). The AFM height profile analysis (see inset of Figure 1(a)) shows that the N-GQDs are mostly of monolayer or bilayer type. The higher magnification TEM image of N-GQDs is shown in Figure 1(b) and HRTEM lattice image of a single N-GQD is shown in the inset of Figure 1(b). The lattice spacing of 0.24 nm corresponds to the (1120) plane of the hexagonal structure of N-GQDs confirming its crystalline nature, consistent with the previous report.[19] The TEM image in Figure 1(c) including a high-resolution image in the inset shows Au NPs with a mostly hexagonal shape and some with pentagonal, triangular and spherical shapes, and these are consistent with the literature.[31-32] The size distribution of Au@N-GQDs with average particle size ~23.4 nm is shown as the inset of Figure 1(c). In Figure 1(d), a good decoration of N-GQDs on the surface of Au NPs is visualized from the HRTEM image. Note that the size of the N-GQDs on Au NP is identical to that of the size of N-GQDs shown in Figure 1(a). The inset of Figure 1(d) shows the lattice fringes of (111) facet of Au NP with interplanar spacing

2.35 Å, which is consistent with the previous report.[31] The decoration of N-GQDs on the Au NP surface is also verified from the elemental mapping in the HAADF and EDX images and the EDX spectrum of a single Au@N-GQD shown in Figure S1 (SI†). The elemental mappings and EDX spectrum confirm the presence of Au, C, O, and N, as expected.

The structure and crystallinity of N-GQDs and Au@N-GQDs are analyzed from XRD spectra, as discussed in section S4 with Figure S2 (SI†). The change in the linewidth is believed to be due to the reduction in the functional groups from the basal plane of GQDs. Further, due to the attachment of Au NPs, the reduction of functional groups in N-GQDs may reduce the interplanar spacing giving rise to higher 2θ (002) peak in Au@N-GQDs.

An overview of the chemical composition of N-GQDs and Au@N-GQDs is presented in Figure 2(a) using the XPS survey scan. Three characteristic peaks at ~284 eV, ~399 eV, and ~531 eV are observed in both N-GQDs and Au@N-GQDs for C 1s, N 1s, and O 1s, respectively,[33] while, the characteristic peak at ~84 eV for Au 4f appears only in Au@N-GQDs[34], as expected. The high-resolution XPS spectra corresponding to C 1s, N 1s, O 1s, and Au 4f are deconvoluted with Gaussian peaks for detailed analysis, as shown in Figure 2(b-h). In the deconvoluted C 1s spectrum in N-GQDs (see Figure 2(b)), the peak at 284.3 eV refers to the graphite-like sp^2 hybridized state (C=C) and the other peaks at 285.5, 287.5 and 288.9 eV are assigned to C=N, C-O, and C=O/ C-N-C functional groups, respectively.[33] For N 1s spectrum of N-GQDs, the binding energy at 397.9, 399.2, 400.7 and 402.7 eV (see Figure 2(c)) are assigned to pyridinic N, pyrrolic N, graphitic N and oxidized state of N as N-O, respectively, which are in good agreement with previous literature .[35-36] The pronounced peaks at 399.2 and 400.7 eV confirm the doping of N atom in N-GQDs. In Figure 2(d), three different peaks at 531.0, 532.1 and 533.5 eV in O 1s spectrum endorse the existence of oxygen-rich functional groups C=O, C-OH/C-O-C and COOH,

respectively[33, 35] in N-GQDs. In the case of Au@N-GQDs, the characteristic Au 4f doublet is deconvoluted with two peaks at 84.4 and 88.1 eV, corresponding to Au $4f_{7/2}$ and Au $4f_{5/2}$ states, respectively, with a spin-orbit splitting of 3.7 eV, as shown in Figure 2(e).[34] Along with the pure metallic Au, the appearance of a peak at 85.8 eV is due to the Au^{+} $4f_{7/2}$ state endorsing the bonding of Au with N-GQDs.[34] In Au@N-GQDs, four different peaks of C 1s appear at 284.3, 285.7, 287.0 and 288.6 eV obtained by the Gaussian deconvolution, as shown in Figure 2(f). As compared to N-GQDs, the contribution of C=C peak increases from 57 % to 63%, while the contribution of N, O related functional groups decreases. This confirms the reduction of defects from the graphitic array after the attachment of Au NPs, consistent with the XRD analysis. It's noteworthy that the reduction in the binding energy of each state of C 1s in Au@N-GQDs, except C=N state confirms the increase of the electron density in the Au@N-GQDs composite. The upshift in the binding energy of C=N from 287.5 eV to 287.7 eV is attributed to the electron donation to Au^{3+} ions at the time of reduction reaction. For N 1s spectrum in Au@N-GQDs (see Figure 2(g)), only pyrrolic N (398.9 eV) and graphitic N (400.5 eV) peaks appear. The disappearance of pyridinic N and N-O peak in Au@N-GQDs revels that these functional groups take a vital role in the reduction of Au^{3+}. The lone pair electrons of the pyridinic N help in the attachment of the Au NPs with N-GQDs and as a result, the discontinuity in graphitic network is filled up leading to the reduction of the defect in N-GQDs, while the presence of huge pyrrolic-N (85%) can increase the n-type conductivity[21] and density of states. In Au@N-GQDs, the modification of the oxidation states of C=O (530.9 eV), C-OH/C-O-C (531.9 eV) and COOH (532.9 eV) functional groups is observed from the deconvoluted O 1s spectrum. The lowering in the binding energy of these functional groups reveals the higher electronic charge density in Au@N-GQDs (see Figure 2(h)). The overall increase of the relative atomic % of C 1s from 54% to 66.8% and the reduction of N 1s and O 1s contribution in

the Au@N-GQDs composite, as listed in Table 1, confirm the reduction of defects and impurities in the graphene structure. Moreover, the deconvoluted high-resolution spectra confirm the modification of the functional groups.

For the further endorsement of the structural characteristics, Raman spectra of as-synthesized N-GQDs and Au@N-GQDs are presented in Figure 3. To acquire insight into the edge states and functional groups, each spectrum is fitted with six Lorentz peaks in the range 1100-1700 cm^{-1}. The details of the peak parameters are tabulated in Table S1 (SI†). The vertical dashed lines on the deconvoluted spectra indicate the positions of D and G bands in N-GQDs at 1365 cm^{-1} and 1590 cm^{-1}, respectively. The D band arises from the structural defects in the sp^2 domain of N-GQDs, whereas the G band in N-GQDs is due to the in-plane phonon vibration of C=C carbon components.[30, 37] In particular, the Raman peak at 1300 cm^{-1} (D_2) is attributed to the O=C-N bond vibration[38], and 1422 cm^{-1} (D_3) for the vibration of C=O/C-O groups[37] confirming the N and O functionalization of N-GQDs. For Au@N-GQDs, a new peak appears at 1528 cm^{-1} due to the Au-C bond formation,[39] confirming the strong coupling between N-GQDs and Au NPs in the Au@N-GQDs composite. As compared to N-GQDs, the redshifts of the G band in Au@N-GQDs from 1590 cm^{-1} to 1585 cm^{-1} is due to the charge transfer [40] from Au NPs to N-GQDs. The enhancement of electron density in N-GQDs is attributed to the increasing polarizability of the Raman active species. This improvement of the polarizability facilitates the redshift of the Raman bands. Interestingly, after the interaction of N-GQDs with Au NPs, an enhancement in the intensity ratio of I_D to I_G (I_D/I_G) from 0.73 to 1.33, accompanied by the reduction of the FWHM of D band and the disappearance of D_3 band (see Table S1, SI†) are observed. The enhancement in D band intensity is primarily due to the preferential attachment of Au NPs at the defect sites of N-GQDs and local enhancement of field due to the plasmonic absorption by Au NPs[39]. In presence of Au

NPs, the intensity of both the G and D bands is increased, with a higher enhancement factor of D band particularly due to the attachment of Au NPs.[39] Thus, the enhancement in D band intensity does not necessarily mean the increase in the defect density. Further, the improvement of D_4 band corresponding to C=N-OH stretching vibration in Au@N-GQDs[38] indicates the modification of the functional groups with –OH groups. A drastic reduction in the FWHM of G band is attributed to the strong vibration of C=C bond in Au@N-GQDs through the enhancement of the local EM field by the SPR absorption of Au NPs[39], confirming the strong coupling between N-GQDs and Au NPs. The Raman analysis confirms the modification of the defect states in N-GQDs as well as the upturn of the charge density in N-GQDs as a result of metal-carbon composites formation, consistent with the XPS analysis. Due to the attachment of Au NP with N-GQDs, the change of the functional groups and modification of different bond vibration are also confirmed from FTIR analysis, as discussed in section S5 with Figure S3 (SI†).

3.2. Optical absorption and photoluminescence studies

In the absorption spectra of Figure 4(a), N-GQDs show a sharp absorption peak at ~262 nm for π-π^* transition of aromatic C=C graphitic components.[30, 41] Though no such distinct peak has been reported for N-GQDs, an extended tail in the absorption spectra from 300-800 nm is reported for the functionalization of N-GQDs with N, O associated functional groups.[14, 42] For the case of Au@N-GQDs, the absorption spectrum exhibits two characteristic absorption peaks, one at ~262 nm for the absorption by N-GQDs and the other at ~547 nm due to the contribution of the surface plasmon resonance (SPR) absorption of Au NPs in the composites, as shown in Figure 4(a). The inset of Figure 4(a) shows the variation of differential absorption ($dA/d\lambda$) with wavelength (λ), which shows two peaks at 320 nm and 380 nm. As compared to bare N-GQDs, the broadening of the absorption tail in Au@N-GQDs composite is detected, which is consistent

with the earlier report.[3] Due to the localized surface plasmon resonance of Au NPs, there is an oscillation of loosely bound electrons that arises on the surface of the nanoparticles under the specific frequency of electromagnetic radiation.[28] Due to this oscillation, the radiation is absorbed around the surface of the nanoparticles, leading to the enhancement of the local optical field which can effectively enhance the absorption in Au@N-GQDs. Note that after the interaction with Au NPs, the reduction of the indirect bandgap of N-GQDs from 3.56 eV to 2.53 eV suggests the strong coupling of Au NPs with N-GQDs, as shown in Figure S4(a) (SI†). Paul et al. reported the reduction of the indirect bandgap of the semiconductor after the strong coupling with metallic NPs.[43] The synthesis of Au NPs with and without the presence of N-GQDs is also monitored to confirm the role of N-GQDs in the synthesis of Au NPs. In the absence of the reducing agent (N-GQDs), the absorption spectrum of the resulting product shows the absence of any SPR peak, as shown in Figure S4(b) (SI†). The addition of N-GQDs is critical to the growth of crystalline Au NPs with a well-defined SPR peak.

Figure 4(b) shows the photoluminescence excitation (PLE) spectra of N-GQDs and Au@N-GQDs with a broad peak centered at ~345 nm for both N-GQDs and Au@N-GQDs, and the PLE peak intensity of Au@N-GQDs is ~12 times higher than that of the N-GQDs. The PLE spectra of Au@N-GQDs is deconvoluted with three Gaussian peaks (see Figure 4(b)). The peak at 266 nm corresponds to the π-π^* transition and the peaks at 326 nm and 375 nm are due to the surface functional groups and the doped atoms, which are fully consistent with the absorption spectrum including differentiated spectrum ($dA/d\lambda$) shown in Figure 4(a).

The PL spectra of N-GQDs and Au@N-GQDs show emission peaks at ~432 nm and ~450 nm, respectively, with 350 nm excitation, as shown in Figure 4(c). The PL intensity of Au@N-GQDs is found to be ~12.1 times stronger than that of the bare N-GQDs measured under identical

conditions, which is consistent with the PLE spectra. The enhancement of PL intensity is comparable to that reported by Majumder et al. for GO wrapped Au nanoplatelets system.[2] To understand the origin of large enhancement of the PL intensity in Au@N-GQDs, the PL spectrum of both N-GQDs and Au@N-GQDs are deconvoluted with three different Gaussian peaks, as presented in Figure 4(c). In N-GQDs, Peak 1 at 425 nm is attributed to the free zigzag edge states excitons[44], peak 2 (472 nm) is for COOH/OH and CN-OH functional groups at the edge [44-46] and peak 3 (510 nm) is due to the presence of oxygen-rich C=O/C-O-C groups.[37] The deconvoluted PL peaks with corresponding functional groups and the relative percentage of the contribution of each fitted peak of N-GQDs and Au@N-GQDs are presented in Table S2 (SI†). No change in the center of peak 1 and 2 for Au@N-GQDs imply that Au NPs do not interact with the free zigzag edge states and COOH/OH groups of N-GQDs, while ~17 nm redshift of peak 3 in Au@N-GQDs indicates the interaction of Au NPs with epoxy groups.[6] Thus, it may be concluded that the functional groups are not responsible for the PL enhancement in Au@N-GQDs. The key factor, which is responsible for the PL enhancement in Au@N-GQDs is the attachment of plasmonic Au NPs with N-GQDs. Owing to the plasmon-enhanced absorption, Au NPs can absorb incident photons and produce coherent collective oscillation of electrons, which decay non-radiatively by the generation of high kinetic energy (~3 eV) hot electrons.[43, 47] Note that the interaction of metallic Au NPs and semiconducting N-GQDs produces a Schottky barrier (Φ_B) at the interface of Au@N-GQDs,[18] as illustrated in Figure 4(d). The energy of the hot electrons is generally higher than the local Schottky barrier height[47], and as a result, the hot electrons are transferred to the conduction band of the semiconductor N-GQDs. It has been reported that the decoration of N-GQDs on the surface of Au NPs is beneficial for the efficient transfer of hot electrons.[47] Since the N-GQDs have lower electron density than the metallic Au NPs, N-GQDs can easily accept the hot electrons.

Further, the work function of GO /GQD (5.86 eV) is reported to be higher than that of the Au NPs (5.20 eV).[48] It has been reported that the presence of functional groups increases the work function of GQD.[49] Hence, due to its lower work function, the electron would be transferred from Au NPs to GQDs. The redshift of the G band clearly indicates the charge (electron) transfer from Au NPs to N-GQDs.[39] Note that the presence of strong electronegative nitrogen atoms further enhances the electron-accepting capability of N-GQDs.[50] Figure 4(d) shows a schematic of the band diagram and the hot electron transfer process in Au@N-GQDs under light illumination. Here, E_{Fs} and E_{Fm} are the Fermi energy level of N-GQDs and Au, respectively, which lie at the same energy level in Au@N-GQDs. E_C and E_V are the conduction and valance band energy level of N-GQDs. Along with the generation of hot electrons in Au NPs, huge numbers of electron-hole pairs are also created in N-GQDs by the enhancement of the overall absorption of N-GQDs with the local field enhancement in the presence of plasmonic Au NPs. Thus, the developed electron density in the conduction band of N-GQDs causes higher recombination and yields a higher intensity of PL in Au@N-GQDs. Despite the charge separation at the metal-semiconductor junction, there is a net increase in the PL intensity, implying that the plasmonic effect surpasses the charge separation effect. For a quantitative analysis of the PL enhancement, the absolute quantum yield was measured by using an integrating sphere. The measured quantum yields are 7.9% and 12.3% for N-GQDs and Au@N-GQDs, respectively. The details of the PL quantum yield measurement are presented in Section S6 (SI†).

Further, the comparison of the TRPL spectra of N-GQDs and Au@N-GQDs in Figure 4(e) shows the average lifetimes of carriers as 5 ns and 6.3 ns, respectively. With the incorporation of Au NPs, slower decay of N-GQDs is consistent with the plasmonic-based system reported earlier.[43] The TRPL spectrum for each sample is fitted well with tri-exponential function:[45] $I(t) =$

$\sum_{i=1}^{3} B_i e^{-\frac{t}{\tau_i}}$, where, I(t) is PL intensity at time t and B_i is the fractional intensity corresponding to decay time τ_i. All fitted parameters for TRPL spectra are tabulated in Table S3 (SI†). The faster decay τ_1 in N-GQDs is due to the band to band transition, whereas, τ_2 and τ_3 are attributed to the interstates to band transitions in N-GQDs.[45] Interestingly, in Au@N-GQDs, τ_1 and τ_2 turned out to be very fast as compared to that of N-GQDs. Since the time constant is inversely proportional to the density of carriers, the decay of the excited state electrons will be faster if the electron density is high. Thus, faster decays in Au@N-GQDs endorse the transfer of hot electrons from Au NPs to the excited state of N-GQDs and the subsequent increase in electron density. In contrast, though the electron density increases in the excited states, the decay time τ_3 increases in Au@N-GQDs. This is primarily due to the charge separation at the Au/N-GQDs junction. The formation of the Schottky barrier at the interface of Au NPs and N-GQDs produces a space charge region in the N-GQDs.[43] This may cause charge separation in N-GQDs resulting in higher exciton stability. Despite the charge separation, we observe an overall increase in the PL intensity with Au NPs due to the reasons discussed above. It is very interesting to note that both faster and slower decay components are present in Au@N-GQDs, which can be beneficial for multi-purpose applications.

3.3. Detection of Fe^{3+} ions by Au@N-GQDs

We have discussed above the high PL QY of Au@N-GQDs with the effective contribution of –OH/COOH functional groups and plasmonic enhancement. Note that due to the high tendency of electron donation, -OH groups can efficiently interact with Fe^{3+} ions [9, 51]. Based on the above, we investigate the Au@N-GQDs as a fluorometric sensor for Fe^{3+} sensing with ultrahigh sensitivity and consequently implemented it for the detection of Fe^{3+} ions in the human serum and river water sample.

The PL spectra of Au@N-GQDs before and after the addition of different concentrations of Fe^{3+} solution were recorded in a wide concentration range (0.001-10 μM) under the excitation of 350 nm with optimized concentration of Au@N-GQDs (101 μg/mL), pH (6), reaction time (12 min) and temperature (20°C), as shown in Figure 5(a). The detailed optimization studies of the sensing parameters are described in section S7 and Figure S5 (SI†). The variation of the relative change in the PL intensity, I/I_0, as a function of the concentration of Fe^{3+} ions is shown in Figure 5(b). Here I_0 and I are the PL intensity of Au@N-GQDs before and after the addition of Fe^{3+} solution. Note that in the present case, the change of the PL intensity of Au@N-GQDs with Fe^{3+} addition does not follow the conventional Stern-Volmer equation, as shown by the dashed line fit to the experimental data in the inset of Figure 5(b). However, over a small concentration range from 0.10 – 0.75 μM, a linear variation of I_0/I with Fe^{3+} can be observed (see Figure S6, SI†) with a limit of detection (LOD) 30 nM and sensitivity 0.33 μM^{-1}. In most of the reported literature, when the variation of the PL intensity of the fluorescence material follows a non-linear behavior with the addition of the quencher, researchers concentrated mainly on the linear portion of the curve to explain the quenching mechanism.[52-53] A quantitative understanding of the non-linearity and better insight into the mechanism of quenching via charge transfer is rarely addressed in the literature.

The exciton decay process in different semiconductors was reported previously with the first-order rate equation[54] Herein, for an in-depth understanding of the quenching phenomena in a wide range of the PL intensity of Au@N-GQDs in presence of Fe^{3+} ions, we use the first-order rate equations to model the charge transfer dynamics as the following:

$$\frac{dN}{dt} = G - [R_1 + R_2(Q)]N \qquad (1a)$$

N is the population of excitons in Au@N-GQDs at any time t. G and R_1 represent the generation rate and decay rate of excitons, respectively. Q represents the concentration of Fe^{3+} ions. $R_2(Q)$ is the rate of charge transfer to Fe^{3+} ions, which is concentration-dependent. Figure 5(c) shows a schematic illustration of different recombination pathways including the charge transfer in Au@N-GQDs from defect levels to Fe^{3+} ions. Due to sub-bandgap excitation used in the present case, the recombination/ decay from the impurity/defects levels is considered here. By solving the rate equation, we obtain

$$N(Q,t) = \frac{1}{R_1+R_2(Q)}\left(G - e^{-(R_1+R_2(Q))t}\right) \qquad (1b)$$

For the steady-state PL measurement, as $t \to \infty$, equation (2a) turns out to be

$$N(Q) = \frac{G}{R_1+R_2(Q)} \qquad (1c)$$

Since the absorption intensity of Au@N-GQDs follows Langmuir's isotherm model with the concentration of Fe^{3+} ions (see Figure S7, SI†), here we use the rate of charge transfer[54] to Fe^{3+} ions as,

$$R_2(Q) = R_2(0)\left(1 - \frac{S}{\alpha Q+1}\right) \qquad (1d)$$

Where S is the charge transfer efficiency and α is the adsorption probability of Fe^{3+} ions with Au@N-GQDs. $R_2(0)$ is the rate of charge transfer at Q = 0. In the Langmuir adsorption model, the adsorbent (in this case Au@N-GQD) is assumed to be an ideal solid surface composed of a series of distinct sites capable of binding the adsorbate (Fe^{3+}). Now the PL intensity of the system is expressed as

$$I(Q) = AN(Q) = \frac{\frac{AG}{R_1+R_2(0)}}{1-\left(\frac{R_2(0)S}{R_1+R_2(0)} \times \frac{1}{\alpha Q+1}\right)} = \frac{B}{1-\frac{C}{\alpha Q+1}} \qquad (1e),$$

where B and C are constants defined as:

$$B = \frac{AG}{R_1+R_2(0)} \qquad (1f), \qquad \text{and} \quad C = \frac{R_2(0)S}{R_1+R_2(0)} \qquad (1g),$$

and A is the collection efficiency of luminescence. In the present case, I/I_0 vs Q graph clearly follows the above equation (1e) (see Figure 5(b)) with fitting constant B = 0.4, C = 0.6 and $\alpha = 0.7$ obtained through iterations. This result reveals that the quenching of the PL intensity of Au@N-GQDs by the charge transfer to Fe^{3+} ions follows the first-order rate equation. Additionally, the high value of the adsorption probability ($\alpha = 0.7$) confirms the high level of interaction between Fe^{3+} ions and Au@N-GQDs. Next, using the value of B and C in equation (1f) and (1g), we obtain $R_2(0) \approx 2R_1$. Thus, the charge transfer to Fe^{3+} is stronger than any other decay process, including radiative recombination. Additionally, with the help of the equation ((1f) and (1g) and fitting parameters, we can conclude that the charge transfer efficiency (S) is > 60% that leads to high quenching in presence of Fe^{3+} ions. Note that high efficiency of charge transfer is enabled by the high quality of the interface between the two species due to the in-situ growth of the heterostructure.

For comparison, the PL spectra of bare N-GQDs and the mixture of N-GQDs and c-Au NPs (synthesized by standard citrated method) (N-GQDs/c-Au NPs) were also considered for Fe^{3+} sensing in the range 0.1-10.0 μM (see Figure S8(a,b), SI†). In presence of 10 μM Fe^{3+} solution, N-GQDs and N-GQDs/Au NPs systems show small quenching of the PL intensity only by ~13% and ~8%, respectively, while the Au@N-GQDs show a very high quenching of ~60%. A comparison of the relative change in the PL intensity, I/I_0 vs. Fe^{3+} concentration in the case of N-GQDs, N-GQDs/c-Au NPs and Au@N-GQDs is shown in Figure S8(c) (SI†). These results demonstrate that the rate of the fluorescence quenching is much higher for Au@N-GQDs with remarkably high sensitivity (1 nM), whereas, the sensitivity of bare N-GQDs and N-GQDs/Au NPs system are 100 nM and 1000 nM, respectively. Note that as compared to other GQD-based

fluorescence sensor, here we achieve as low as 1 nM LOD for the sensing of Fe^{3+} ion with Au@N-GQDs, as listed in Table 2.

3.4. Mechanism of Fe^{3+} sensing

Based on the above, we discuss the possible mechanisms behind the ultrahigh sensitivity of Au@N-GQDs towards Fe^{3+} detection and provide experimental verification of the same through further characterizations. Following may be the key factors: First, due to the higher affinity of Au NPs to the functional groups of the basal planes of N-GQDs, the edge functional groups of Au@N-GQDs are not only easily accessible but also well separated from each, which is beneficial for efficient and mass interaction with Fe^{3+}. Second, a higher contribution of -OH edge functional groups in Au@N-GQDs causes well coordination with Fe^{3+} ions. Third, due to the high electron-donating property of -OH groups in Au@N-GQDs, electron-rich Au@N-GQDs transfer electrons to the half-filled 3d-orbit of Fe^{3+} ions for their neutralization. Fourth, the long-lived excitons in Au@N-GQDs can help in the efficient interaction and photoinduced charge transfer to Fe^{3+} ions. Through the strong coordination with -OH functional groups in Au@N-GQDs, N-GQDs transfer photo-induced electrons to Fe^{3+}, facilitating more charge separation and reduced radiative recombination in Au@N-GQDs. Due to the interaction of Fe^{3+} ions with the functional group of Au@N-GQDs, Au@N-GQDs get agglomerated after interfacing with Fe^{3+}, as visualized through the TEM imaging (see Figure S9(a,b), SI†). TEM elemental mapping and EDX analysis confirmed the presence of Fe^{3+} in the Au@N-GQDs/Fe^{3+} composite (see Figure S9(c-h), SI†). Further, the FTIR analysis reveals the reduction of bending vibration of O-H groups at 1352 cm^{-1} (see Figure S10, SI†), due to the complex formation between Fe^{3+} ions and -OH groups in Au@N-GQDs. A comparison of the Raman spectra without and with Fe in Figure S11(a) (SI†) shows that the intensity of D band decreases drastically after the addition of Fe^{3+} ions in Au@N-GQDs,

confirming the complex formation between the functional groups Au@N-GQDs and Fe^{3+}. Further, the redshift of the G band from 1585 cm^{-1} to 1581 cm^{-1} (see Figure S11(b), SI†) reveals higher charge transfer from Au NPs to N-GQDs in presence of Fe^{3+}, confirming the photoinduced charge transfer to Fe^{3+} via N-GQDs. Additionally, the redshift of the D band position in Au@N-GDQs/Fe^{3+} by 14 cm^{-1} with respect to that of Au@N-GQDs reveals that Fe^{3+} mainly interacts with the functional groups of Au@N-GQDs for the charge transfer. The systematic reduction of the N-GQDs absorption, consistent with the PL quenching, confirms the Au@N-GQDs/Fe^{3+} complex formation through N-GQDs, whereas, the diminution of the intensity of SPR absorption peak of Au@N-GQDs confirm the charge transfer phenomena (see Figure S7(a), SI†). Interestingly, in the presence of Fe^{3+} ions, the photocurrent is reduced by nearly 5 times as evident from Figure S12(a) (SI†). With 405 nm laser excitation, the photogenerated charge carriers are transferred from Au@N-GQDs to the unfilled orbits of Fe^{3+} ions before reaching to the electrode, and consequently, the photocurrent is diminished. These results endorse that Fe^{3+} ions quench the PL intensity of Au@N-GQDs by the photoinduced charge transfer process. In the presence of Fe^{3+}, the PL lifetime is increased from 6.3 ns to 12 ns, which implies a dynamic quenching process through the stronger charge separation (see Figure 5(d)). It is also found that in the presence of Fe^{3+}, PL lifetime of N-GQDs is increased (see Figure S12(b), SI†), signifying the photoinduced charge separation via N-GQDs. For the case of Au@N-GQDs, higher electron density with more stable exciton facilitates more interaction possibilities with Fe^{3+} following the charge separation. Note that in the case of N-GQDs/c-Au NPs, no appreciable change in the lifetime was observed after the addition of Fe^{3+} (see Figure S12(c), SI†).

For a better understanding, the temporal change of the PL intensity with reaction time (t) is shown in Figure S5(c) (SI†), and it is fitted with two distinct sequential exponents. Just after

mixing of Fe^{3+} with Au@N-GQDs, as there is insufficient time for Au@N-GQDs/Fe^{3+} complex formation, the inefficient charge transfer causes slower quenching ($e^{-t/1.9}$), while the fast temporal PL decay in the second region ($e^{-t/1.3}$) is attributed to the efficient charge transfer, accelerated by the Au@N-GQDs/Fe^{3+} complex formation. This analysis shows that the quenching of PL intensity of Au@N-GQDs is assisted by the photoinduced charge transfer to Fe^{3+} ions followed by Au@N-GQDs/Fe^{3+} complex formation.

To better understand the nature of the complex formation between Fe^{3+} ions and Au@N-GQDs, the change of the PL intensity of the complex is investigated by the addition of Ethylenediaminetetraacetic acid (EDTA, Sigma Aldrich) at different concentrations (0.5-10 μM), as shown in Figure S13(a) (SI†). With the addition of EDTA, the PL intensity of Au@N-GQDs increases. The inset shows the variation of the recovered PL intensity of Au@N-GQDs with EDTA concentration. With 10 μM concentration of EDTA, the PL intensity of Au@N-GQDs is recovered up to 91% of its original value. Due to the higher stability of Fe^{3+}-EDTA (log $K_{Fe\text{-}EDTA}$ =25)[55], Fe^{3+} makes chelation with EDTA triggering the disaggregation of Au@N-GQDs and the PL of Au@N-GQDs is restored. For further confirmation, the recovery of the lifetime (from τ_{avg} ~12 ns to τ_{avg} ~8.2 ns) of Au@N-GQDs in the presence of 10 μM EDTA is also demonstrated with the addition of 5 μM Fe^{3+} (see, Figure S13(b), SI†). The recovery of each component of the decay time (see Table S3, SI†) after the detachment of Fe^{3+} endorses that the PL quenching of Au@N-GQDs occurs due to the extraction of electrons from the excited state of Au@N-GQDs by Au@N-GQD/Fe^{3+} complex formation. These studies confirm that the quenching of the PL of Au@N-GQDs is caused by the excited state electron transfer through the interaction with the edge functional groups of N-GQDs resulting in the aggregation of Au@N-GQDs. It is worth mentioning that the reversibility of the fluorescent probe makes it extremely useful for practical applications.

3.5. Fe^{3+} sensing in real-life samples

Due to its ultrahigh sensitivity for the detection of Fe^{3+}, Au@N-GQDs has great potential in real sample analysis. However, before its use in real samples, the selectivity test is highly desirable. For this purpose, several other possible co-existing ions of Fe^{3+}, such as Na^{+}, Mn^{2+}, Mg^{2+}, Cs^{+}, Cd^{2+}, Cr^{3+}, Sn^{2+}, Zn^{2+}, Ag^{+}, Co^{2+}, Cu^{2+}, Hg^{2+}, Pb^{2+} and Al^{3+} of 10 μM concentration were added to Au@N-GQDs solution under identical experimental condition. Figure 6(a) presents the relative change of the PL intensity (I_0/I) of Au@N-GQDs with different interfering species, where only Fe^{3+} can show the proficient quenching of the PL intensity, confirming the high selectivity towards Fe^{3+}. As compared to other metal ions, the overlap of the $FeCl_3$ absorption and the PL spectra of Au@N-GQDs (see Figure 6(b)) facilitate efficient photoinduced charge transfer leading to higher selectivity towards Fe^{3+} ions.

For the detection of Fe^{3+} in human serum, the human blood serum was 100-fold diluted with PBS buffer (pH 6) and added with the Au@N-GQDs solution. Next, different known concentrations of Fe^{3+} (0.05, 0.5, 5 μM) were spiked with the Au@N-GQDs solution, and then the concentration of Fe^{3+} ions was determined by the standard addition method. The change in the PL intensity with spiked Fe^{3+} concentration in the serum sample is shown in Figure S14(a) (SI†). To evaluate the Au@N-GQDs based Fe^{3+} sensors in different aqueous systems, river water was collected from river Brahmaputra, Guwahati, India. The tap water and drinking water were collected from the laboratory basin and RO water purifier (Kent), respectively. Each water sample was simply filtered with a 0.22 μm membrane without any further processing. Following a similar procedure as for serum preparation, Au@N-GQDs solutions in different water samples were prepared after 20 times dilution of each sample. Figure S14(b-d) (SI†) shows the change of the PL intensity with the spiked Fe^{3+} concentration in river water, tap water, and drinking water samples.

In each case, sensing of Fe^{3+} ions is evident from the quenching of fluorescence. The satisfactory recovery of Fe^{3+} ions in different real samples, as shown in Table S4 (SI†) holds great potential for Au@N-GQDs as an efficient biosensor as well as an environmental sensor.

3.6. Performance of Au@N-GQDs as a high-speed Schottky junction photodetector

The enhancement of the absorption in entire UV-Vis-NIR and higher exciton stability with high charge density in Au@N-GQDs dictates us to explore its application as a photodetector. Herein, Au@N-GQDs composite is utilized to demonstrate its efficacy as an ultrafast Schottky junction photodetector. Figure 7(a) illustrates the device configuration with an optical image of the patterned Al electrodes on top of Au@N-GQDs film. Here, the electrical characteristics of the device were measured at room temperature by applying a voltage (V) to the Al top contact. Figure 7(b) shows the cross-sectional view of ~80 nm thick layer of Au@N-GQDs on the SiO_2/Si substrate. For comparison, an identical device was also fabricated with the bare N-GQDs layer. The I-V characteristics of Au@N-GQDs in Figure 7(c) show a asymmetric nonlinear behavior for the positive and negative bias voltages for both dark and light conditions, suggesting a back-to-back Schottky diode-like behavior. Figure 7(d) depicts the time-dependent photoresponses of Au@N-GQDs device upon the light on/off intervals of 2.67 ms under 405 nm laser excitation with an illumination power of 3.68 mW/cm^2 at different bias voltage (-5V, -7V and -10 V). The induced photocurrent is clearly proportional to the applied bias voltage. The ultrafast reversibility of the ON-OFF switching of Au@N-GQDs device over several cycles shows remarkable repeatability and robustness of the device. With the decoration of N-GQDs on Au NPs surface, a high-performance photodetector is achieved in the present work. Note that in N-GQDs, a minimum -5V bias is required to get an appreciable photocurrent (see Figure S15(a), SI†). In contrast, the

Au@N-GQDs device can be operated with as low as -1 V bias, confirming the stronger intrinsic charge separation in Au@N-GQDs. Note that at zero bias, no measurable photocurrent is observed for Au@N-GQDs, even at high excitation intensity. Despite the light-induced charge separation in Au@N-GQDs, an intrinsic property of metal/semiconductor junction, the charge carriers do not get sufficient energy to reach up to the electrodes under zero bias, while the photocurrent is appreciable for Au@N-GQDs photodetector at -1 V, which is superior to that of the N-GQD based photodetectors reported earlier.[18-19, 24] At -5 V, the photocurrent is reasonably high for Au@N-GQDs photodetector as compared to that of N-GQDs device. As compared to N-GQDs, the enormous increase of the photocurrent in Au@N-GQDs can be attributed to the enhanced near field oscillation of electrons in Au NPs, which increases the carrier density in Au@N-GQDs by the hot electrons in Au NPs and electron-hole separation in N-GQDs. It is worth mentioning that after one month of the device fabrication, the ratio of I_{ON} and I_{OFF} is unchanged, revealing the high stability of the Au@N-GQDs based photodetector. One of the performance parameters of a photodetector is the photoresponse time/speed. The ultrafast photoresponse of Au@N-GQDs was measured using a digital storage oscilloscope. High-resolution photoresponse curve of Au@N-GQDs photodetector with a 405 nm pulsed laser excitation is presented in Figure 7(e). The laser source could be modulated up to a frequency of 10 kHz with external TTL. To estimate the characteristic rise/fall time of the Au@N-GQDs photodetector, the photoresponse curve is fitted with the exponential rise and decay functions as:[56-57] $I_r(t) = I_{0r} + A_1(1 - e^{-\frac{t}{t_r}})$ and $I_f(t) = I_{0f} + B_1 e^{-\frac{t}{t_f}}$, where, $I_r(t)$ and $I_f(t)$ are the photocurrent with time t for rising and falling edges, respectively. I_{0r} and I_{0f}, A_1, B_1 are the constant. t_r and t_f are the rise and fall time, respectively. The value of t_r and t_f for Au@N-GQDs are found as 23 μs and 100 μs, respectively, through the fitting. As compared to the performance of GQDs based photodetectors reported till date, our Au@N-

GQDs based device shows much faster response.[18, 24] The fast rise time (23 μs) is due to the built-in potential at the Au NPs and N-GQDs junction and a comparatively slower decay of the photocurrent with fall time of 100 μs is attributed to defect states in N-GQDs of Au@N-GQDs. In contrast, the response time of bare N-GQDs is much slower, and it is calculated as t_r = 302 ms and t_f = 208 ms from the photoresponse data presented in Figure S15(b) (SI†). A schematic illustration of the energy band diagram explaining the generation of photocurrent in Au@N-GQDs junction is presented in Figure 7(f). When a Schottky junction is formed between the metal and semiconductor, a built-in potential V_0 appears on the semiconductor side due to the alignment of the Fermi levels. Correspondingly, an electric field directed from N-GQDs to Au NPs in the space charge region of the Schottky junction causes energy bands bending on the semiconductor side.[43] With the external reverse bias V_{ex}, the potential increases to (V_0+V_{ex}) which enable further band bending in the semiconducting side and the increase in width of the space charge region and electric field in the Schottky junction. Due to higher band bending in N-GQDs under reverse bias, the Fermi level of N-GQDs goes down as compared to that of the Au NPs (see Figure 7(f)), which helps in the efficient transfer of hot electrons. Also, the enhancement of the electric field drifts the charge carrier towards the opposite electrodes and causes a high photocurrent. Under reverse bias condition, the flow of electrons and holes are depicted in Figure 7(f). Thus, with the incident illumination, the probability of recombination of carriers is very low under external reverse bias, and it results in high photocurrent in the Au@N-GQDs device. As compared to N-GQDs, the ultrafast photoresponse of Au@N-GQDs is attributed to faster charge separation at the Schottky junction. It is well known that for a moderate to high doping case, the depletion width is ~0.1 μm at the metal/semiconductor interface. In the present case, the thickness of the individual N-GQD is ~0.4 nm, as confirmed from the AFM height profile. Thus, due to the ultralow thickness of the

semiconducting N-GQD region, the carriers can transfer from one side to other by tunneling, besides the hot-electron transfer at the Schottky junction. This tunneling is believed to contribute to the fast photoresponse in the Au@N-GQDs device. The attachment of Au NPs with N-GQDs also helps to reduce the defects in N-GQDs (as confirmed from XRD, XPS and Raman analysis) as well as the surface modification with functional groups also helps to reduce the trapping states and increase the mobility of the charge carrier in N-GQDs resulting in the fast photoresponse. Furthermore, the large mean free path of electrons in Au NPs helps in efficient hot electron transfer to N-GQDs[47], and in Au@N-GQDs the plasmon-induced electromagnetic field causes an efficient separation of photogenerated charge carriers.[58] Additionally, the presence of oxygen-rich functional groups in Au@N-GQDs helps to produce a low resistance path by reducing the local Schottky barrier height at the metal/semiconductor interfaces.[59] It's noteworthy that the response speed of the Au@N-GQDs photodetector is much superior to that of the previously developed GQD based photodetector with and without the use of the transporting layer, as listed in Table 3. Further, the responsivity of Au@N-GQDs photodetector is much higher than that of typical commercial photodetector based on Si.

To investigate the quantitative dependence of the photocurrent with the illumination intensity, the photocurrent of Au@N-GQDs device is measured for different powers of 405 nm laser, as shown in Figure 8(a). The dependence of photocurrent on the incident powder can be fitted by a simple power-law equation:[26] $I_{ph} = BP_{in}^{\alpha}$, where photocurrent I_{ph}, P_{in} is the incident light power density, B is constant, and α is the exponent. The power equation fits the experimental data with an exponent $\alpha = 0.98$, as shown in the inset of Figure 8(a). This linear variation of the photocurrent with laser power for Au@N-GQDs photodetector reveals that the amount of

photogenerated carriers is nearly proportional to the absorbed photon flux,[26] implying a low recombination probability in Au@N-GQDs.

To characterize the performance of the as-fabricated photodetectors, the figure of merit parameters of responsivity (R(λ)), detectivity (D) and external quantum efficiency (EQE) are evaluated in the spectral range 380-800 nm at 5 V bias condition for both N-GQDs and Au@N-GQDs. R(λ) indicates the response efficiency of a detector with a specific optical signal, and it is estimated according to the following equation[60]: $R(\lambda) = \frac{I_{ph}}{P_{in}A}$, where, I_{ph} is the photocurrent, and A is the effective illuminated area (in the present case, A is 0.01 cm^2). The comparative spectral responsivity of N-GQDs and Au@N-GQDs is shown in Figure 8(b). Bare N-GQDs exhibit a broadband response (UV-Vis region) with a responsivity ~0.103 A/W, while Au@N-GQDs shows relatively high spectral response with a peak responsivity 1.36 A/W at 580 nm. Thus, the responsivity of Au@N-GQDs is ~14 times higher than that of bare N-GQDs. Note that the photo responsivity peak position is near to its plasmonic absorption peak (~547 nm), strongly suggesting that the superior performance of Au@N-GQDs photodetector mainly originates from the plasmon resonance-enhanced absorption and subsequent hot electron generation. It's noteworthy that the present device without any charge transporting layer shows superior performance than the transporting layer-based GQDs system reported previously.[24]

Next, the detectivity of the photodetector was calculated using the relation:[26] $D = R(\lambda)(\frac{A}{2QI_D})^{1/2}$, where, Q is the electronic charge (1.6×10^{19} C). The I_D is the dark current. The detectivity of N-GQDs and Au@N-GQDs are estimated as 1.5×10^{10} Jones and 2.03×10^{11} Jones at 580 nm, respectively at 5V bias (see Figure 8(c)). Thus, the detectivity of Au@N-GQDs based photodetector is ~13.5 times higher than that of the bare N-GQDs based device. Based on the

literature reports, we find that Au@N-GQDs based photodetector processes superior performance in comparison to other GQD based photodetectors, as summarized in Table 3.

Similarly, the EQE is calculated using the relation:[26] $EQE(\%) = 100\frac{1240\,R(\lambda)}{\lambda}$. For N-GQDs, the highest value of EQE is 24.4% at 420 nm, while that of Au@N-GQDs is 292.2% at 580 nm, as shown in Figure 8(d). The large value of EQE larger than 100% is attributed to the tunneling of the electrons from Au NPs to N-GQDs through the thin depletion region at the Au/ N-GQD interface. Further, under the reverse bias, as the holes of N-GQDs moves towards the metal/semiconductor interface, as illustrated in Figure 7(f), the hole trapping at the interface may thins down the depletion region[61] and causes more charge tunneling to N-GQDs.

4. Conclusions

In summary, we have demonstrated an in-situ growth of Au@N-GQDs heterostructure with superior performance for metal ion sensing and photodetection applications. Au@N-GQDs are implemented as a label-free sensor of Fe^{3+} ions with ultrahigh sensitivity and selectivity. The unusual quenching of fluorescence of Au@N-GQDs in the presence of Fe^{3+} ions is modeled by solving analytical rate equations incorporating Langmuir's law of adsorption and nonradiative charge transfer to the acceptor ions, for the first time. Further, the newly developed sensor is successfully implemented for the detection of Fe^{3+} ions in human serum and real water samples, including Brahmaputra river water with satisfactory recovery. Next, we demonstrate the fabrication of Au@N-GQDs based planar photodetector with ultrafast photoresponse and high photoresponsivity. The incorporation of plasmonic Au NPs in the Au@N-GQDs system generates hot electrons and transfers these to N-GQDs to achieve high photocurrent. Additionally, through the attachment of the Au NPs on the basal plane of N-GQDs, the defect states are reduced along

with the modification of the edge functional groups as well as the tunneling of electrons through the thin depletion region cause the ultrafast photoresponse (~10^4 times faster than bare N-GQDs) in Au@N-GQDs. A high spectral responsivity of 1.36 A/W at 580 nm is achieved in Au@N-GQDs photodetector by the plasmonic effect, and it is ~14 times higher than that of the bare N-GQDs. The manifold applications of Au@N-GQDs grown by a green approach open up the versatility of Au@N-GQDs in the biomedical and optoelectronic research fields.

Supporting Information

GO and N-GQDs synthesis, characterization techniques, photoresponse measurements set up, HAADF image and the corresponding mapping of Au@N-GQDs, comparison of N-GQDs and Au@N-GQDs in XRD and FTIR spectra, optimization of sensing parameters for the detection of Fe^{3+} ions and the corresponding characterizations and tables, PL spectra for comparison of quenching and real sample analysis, photocurrent for N-GQDs, Table of fitting parameters of Raman spectra, PL spectra and TRPL spectra.

Acknowledgments

We acknowledge the financial support from MEITY (Grant No. 5(9)/2012-NANO (VOL-II)) for carrying out part of this work. Central Instruments Facility, I.I.T. Guwahati is acknowledged for providing the TEM, FESEM, Raman and TRPL facilities. We gratefully acknowledge Dr. W. Theis and Mr. A. J. Pattison, University of Birmingham, for their valuable support with the HAADF-STEM imaging.

References:

(1) Tian, L.; Ghosh, D.; Chen, W.; Pradhan, S.; Chang, X.; Chen, S. Nanosized Carbon Particles from Natural Gas Soot. *Chemistry Of Materials* **2009,** *21*, 2803-2809.

(2) Majumder, S.; Satpati, B.; Kumar, S.; Banerjee, S. Multifunctional Reduced Graphene Oxide Wrapped Circular Au Nanoplatelets: Enhanced Photoluminescence, Excellent Surface-Enhanced Raman Scattering, Photocatalytic Water Splitting, and Non-Enzymatic Biosensor. *ACS Appl. Nano Mater.* **2018,** *1*, 3945-3955.

(3) Ju, J.; Chen, W. In situ growth of surfactant-free gold nanoparticles on nitrogen-doped graphene quantum dots for electrochemical detection of hydrogen peroxide in biological environments. *Anal. Chem.* **2015,** *87*, 1903-1910.

(4) Yan, X.; Li, Q.; Li, L.-s. Formation and Stabilization of Palladium Nanoparticles on Colloidal Graphene Quantum Dots. *J. Am. Chem. Soc.* **2012,** *134*, 16095-16098.

(5) Star, A.; Joshi, V.; Skarupo, S.; Thomas, D.; Gabriel, J.-C. P. Gas Sensor Array Based on Metal-Decorated Carbon Nanotubes. *J. Phys. Chem. B* **2006,** *110*, 21014-21020.

(6) Melo, J. P.; Ríos, P. L.; Povea, P.; Morales-Verdejo, C.; Camarada, M. B. Graphene Oxide Quantum Dots as the Support for the Synthesis of Gold Nanoparticles and Their Applications as New Catalysts for the Decomposition of Composite Solid Propellants. *ACS Omega* **2018,** *3*, 7278-7287.

(7) Li, S.; Li, Y.; Cao, J.; Zhu, J.; Fan, L.; Li, X. Sulfur-doped Graphene Quantum Dots as a Novel Fluorescent Probe for Highly Selective and Sensitive Detection of Fe3+. *Anal. Chem.* **2014,** *86*, 10201-10207.

(8) Cui, X.; Wang, Y.; Liu, J.; Yang, Q.; Zhang, B.; Gao, Y.; Wang, Y.; Lu, G. Dual Functional N-and S-Co-doped Carbon Dots as the Sensor for Temperature and Fe3+ Ions. *Sensors and Actuators B: Chemical* **2017,** *242*, 1272-1280.

(9) Ma, Q.; Song, J.; Wang, S.; Yang, J.; Guo, Y.; Dong, C. A General Sensing Strategy for Detection of Fe3+ By Using Amino Acid-Modified Graphene Quantum Dots as Fluorescent Probe. *Appl Surf Sci* **2016,** *389*, 995-1002.

(10) Xu, H.; Zhou, S.; Xiao, L.; Wang, H.; Li, S.; Yuan, Q. Fabrication of a Nitrogen-doped Graphene Quantum Dot from MOF-Derived Porous Carbon and its Application for Highly Selective Fluorescence Detection of Fe 3+. *J. Mater. Chem. C* **2015,** *3*, 291-297.

(11) Ajlec, R.; Štupar, J. Determination of Iron Species in Wine by Ion-Exchange Chromatography-Flame Atomic Absorption Spectrometry. *Analyst* **1989,** *114*, 137-142.

(12) Chinoporos, E. Detection of Ferric Ions with 4, 4'-Dicarboxydicyclohexylamine. *Analytical Chemistry* **1962,** *34*, 437-438.

(13) Ananthanarayanan, A.; Wang, X.; Routh, P.; Sana, B.; Lim, S.; Kim, D. H.; Lim, K. H.; Li, J.; Chen, P. Facile Synthesis of Graphene Quantum Dots from 3D Graphene and their Application for Fe3+ Sensing. *Adv. Funct. Mater.* **2014,** *24*, 3021-3026.

(14) Wu, P.; Li, W.; Wu, Q.; Liu, Y.; Liu, S. Hydrothermal Synthesis of Nitrogen-doped Carbon Quantum Dots from Microcrystalline Cellulose for the Detection of Fe 3+ Ions in an Acidic Environment. *RSC Adv.* **2017,** *7*, 44144-44153.

(15) Guo, R.; Zhou, S.; Li, Y.; Li, X.; Fan, L.; Voelcker, N. H. Rhodamine-functionalized Graphene Quantum Dots for Detection of Fe3+ in Cancer Stem Cells. *ACS Appl. Mater. Interfaces* **2015,** *7*, 23958-23966.
(16) Long, M.; Wang, P.; Fang, H.; Hu, W. Progress, Challenges, and Opportunities for 2D Material Based Photodetectors. *Advanced Functional Materials* **2019,** *29*, 1803807-1803835.
(17) Jin, Z.; Owour, P.; Lei, S.; Ge, L. Graphene, Graphene Quantum Dots and their Applications in Optoelectronics. *Curr. Opin. Colloid Interface Sci.* **2015,** *20*, 439-453.
(18) Zhang, Q.; Jie, J.; Diao, S.; Shao, Z.; Zhang, Q.; Wang, L.; Deng, W.; Hu, W.; Xia, H.; Yuan, X. Solution-processed Graphene Quantum Dot Deep-UV Photodetectors. *ACS nano* **2015,** *9*, 1561-1570.
(19) Dey, T.; Mukherjee, S.; Ghorai, A.; Das, S.; Ray, S. K. Surface State Selective Tunable Emission of Graphene Quantum Dots exhibiting Novel Thermal Quenching Characteristics. *Carbon* **2018,** *140*, 394-403.
(20) Du, Y.; Guo, S. Chemically Doped Fluorescent Carbon and Graphene Quantum Dots for Bioimaging, Sensor, Catalytic and Photoelectronic Applications. *Nanoscale* **2016,** *8*, 2532-2543.
(21) Ma, C. B.; Zhu, Z. T.; Wang, H. X.; Huang, X.; Zhang, X.; Qi, X.; Zhang, H.-L.; Zhu, Y.; Deng, X.; Peng, Y. A General Solid-State Synthesis of Chemically-doped Fluorescent Graphene Quantum Dots for Bioimaging and Optoelectronic Applications. *Nanoscale* **2015,** *7*, 10162-10169.
(22) Cheng, S.-H.; Weng, T.-M.; Lu, M.-L.; Tan, W.-C.; Chen, J.-Y.; Chen, Y.-F. All Carbon-based Photodetectors: An Eminent Integration of Graphite Quantum Dots and Two dimensional Graphene. *Sci. Rep.* **2013,** *3*, 2694-2701.
(23) Tetsuka, H.; Nagoya, A.; Tamura, S.-i. Graphene/Nitrogen-functionalized Graphene Quantum Dot Hybrid Broadband Photodetectors with a Buffer Layer of Boron Nitride Nanosheets. *Nanoscale* **2016,** *8*, 19677-19683.
(24) Kim, C. O.; Hwang, S. W.; Kim, S.; Shin, D. H.; Kang, S. S.; Kim, J. M.; Jang, C. W.; Kim, J. H.; Lee, K. W.; Choi, S.-H. High-Performance Graphene-Quantum-Dot Photodetectors. *Sci. Rep.* **2014,** *4*, 5603-5609.
(25) Nguyen, D. A.; Oh, H. M.; Duong, N. T.; Bang, S.; Yoon, S. J.; Jeong, M. S. Highly Enhanced Photoresponsivity of a Monolayer Wse2 Photodetector with Nitrogen-doped Graphene Quantum Dots. *ACS Appl. Mater. Interfaces* **2018,** *10*, 10322-10329.
(26) Mihalache, I.; Radoi, A.; Pascu, R.; Romanitan, C.; Vasile, E.; Kusko, M. Engineering Graphene Quantum Dots for Enhanced Ultraviolet and Visible Light P-Si Nanowire-based Photodetector. *ACS Appl. Mater. Interfaces* **2017,** *9*, 29234-29247.
(27) Kim, M.; Kang, P.; Leem, J.; Nam, S. A Stretchable Crumpled Graphene Photodetector with Plasmonically Enhanced Photoresponsivity. *Nanoscale* **2017,** *9*, 4058-4065.
(28) Liu, Y.; Cheng, R.; Liao, L.; Zhou, H.; Bai, J.; Liu, G.; Liu, L.; Huang, Y.; Duan, X. Plasmon Resonance Enhanced Multicolour Photodetection by Graphene. *Nat. Commun.* **2011,** *2*, 579-586.
(29) Du, B.; Lin, L.; Liu, W.; Zu, S.; Yu, Y.; Li, Z.; Kang, Y.; Peng, H.; Zhu, X.; Fang, Z. Plasmonic Hot Electron Tunneling Photodetection in Vertical Au–Graphene Hybrid Nanostructures. *Laser & Photonics Reviews* **2017,** *11*, 1600148-1600155.
(30) Das, R.; Rajender, G.; Giri, P. K. Anomalous Fluorescence Enhancement and Fluorescence Quenching of Graphene Quantum Dots by Single Walled Carbon Nanotubes. *Phys. Chem. Chem. Phys.* **2018,** *20*, 4527-4537.
(31) Das, R.; Paul, K. K.; Giri, P. K. Highly Sensitive and Selective Label-Free Detection of Dopamine in Human Serum based on Nitrogen-Doped Graphene Quantum Dots Decorated on Au Nanoparticles: Mechanistic Insights Through Microscopic and Spectroscopic Studies. *Appl Surf Sci* **2019,** 490, 318-330.
(32) Palui, G.; Ray, S.; Banerjee, A. Synthesis of Multiple Shaped Gold Nanoparticles using Wet Chemical Method by Different Dendritic Peptides at Room Temperature. *J. Mater. Chem.* **2009,** *19*, 3457-3468.
(33) Parvizi, R.; Azad, S.; Dashtian, K.; Ghaedi, M.; Heidari, H. Natural Source-Based Graphene as Sensitising Agents for Air Quality Monitoring. *Sci. Rep.* **2019,** *9*, 3798-3813.

(34) Sierra, J. A.; Vanoni, C. R.; Tumelero, M. A.; Cid, C. C. P.; Faccio, R.; Franceschini, D. F.; Creczynski-Pasa, T. B.; Pasa, A. A. Biogenic Approaches using Citrus Extracts for the Synthesis of Metal Nanoparticles: The Role of Flavonoids in Gold Reduction and Stabilization. *New J. Chem.* **2016,** *40*, 1420-1429.
(35) Qu, D.; Sun, Z.; Zheng, M.; Li, J.; Zhang, Y.; Zhang, G.; Zhao, H.; Liu, X.; Xie, Z. Three Colors Emission from S,N Co-doped Graphene Quantum Dots for Visible Light H2 Production and Bioimaging. *Adv. Opt. Mater.* **2015,** *3*, 360-367.
(36) Lu, X.; Wang, D.; Ge, L.; Xiao, L.; Zhang, H.; Liu, L.; Zhang, J.; An, M.; Yang, P. Enriched graphitic N in nitrogen-doped graphene as a superior metal-free electrocatalyst for the oxygen reduction reaction. *New J. Chem.* **2018,** *42*, 19665-19670.
(37) Rajender, G.; Giri, P. K. Formation Mechanism of Graphene Quantum Dots and their Edge State Conversion Probed by Photoluminescence and Raman Spectroscopy. *J. Mater. Chem. C* **2016,** *4*, 10852-10865.
(38) Socrates, G. Infrared and Raman Characteristic Group Frequencies: Tables and Charts, John Wiley & Sons: 2004.
(39) Biroju, R. K.; Giri, P. K. Defect Enhanced Efficient Physical Functionalization of Graphene with Gold Nanoparticles Probed by Resonance Raman Spectroscopy. *J. Phys. Chem. C* **2014,** *118*, 13833-13843.
(40) Paul, K. K.; Sreekanth, N.; Biroju, R. K.; Pattison, A. J.; Escalera-López, D.; Guha, A.; Narayanan, T. N.; Rees, N. V.; Theis, W.; Giri, P. K. Strongly Enhanced Visible Light Photoelectrocatalytic Hydrogen Evolution Reaction in An N-Doped Mos2/Tio2 (B) Heterojunction by Selective Decoration of Platinum Nanoparticles at the Mos2 Edge Sites. *J. Mater. Chem. A* **2018,** *6*, 22681-22696.
(41) Hu, S.; Trinchi, A.; Atkin, P.; Cole, I. Tunable Photoluminescence Across the Entire Visible Spectrum From Carbon Dots excited by White Light. *Angew. Chem.* **2015,** *54*, 2970-2974.
(42) Govindaraju, S.; Ankireddy, S. R.; Viswanath, B.; Kim, J.; Yun, K. Fluorescent Gold Nanoclusters for Selective Detection of Dopamine in Cerebrospinal Fluid. *Sci. Rep.* **2017,** *7*, 40298-40310.
(43) Paul, K. K.; Giri, P. K. Role of Surface Plasmons and Hot Electrons on the Multi-Step Photocatalytic Decay by Defect Enriched Ag@ Tio2 Nanorods under Visible Light. *J. Phys. Chem. C* **2017,** *121*, 20016-20030.
(44) Du, J.; Wang, H.; Wang, L.; Zhu, S.; Song, Y.; Yang, B.; Sun, H. Insight into the Effect of Functional groups on Visible-Fluorescence Emissions of Graphene Quantum Dots. *J. Mater. Chem. C* **2016,** *4*, 2235-2242.
(45) Kumar, G. S.; Roy, R.; Sen, D.; Ghorai, U. K.; Thapa, R.; Mazumder, N.; Saha, S.; Chattopadhyay, K. K. Amino-Functionalized Graphene Quantum Dots: Origin of Tunable Heterogeneous Photoluminescence. *Nanoscale* **2014,** *6*, 3384-3391.
(46) Lee, E.; Ryu, J.; Jang, J. Fabrication of Graphene Quantum Dots via Size-Selective Precipitation and their Application in Upconversion-based Dsscs. *ChemComm* **2013,** *49*, 9995-9997.
(47) Gosciniak, J.; Atar, F. B.; Corbett, B.; Rasras, M. Plasmonic Schottky Photodetector with Metal Stripe Embedded into Semiconductor and with a CMOS-Compatible Titanium Nitride. *Sci. Rep.* **2019,** *9*, 6048-6060.
(48) Khoa, N. T.; Kim, S. W.; Yoo, D.-H.; Kim, E. J.; Hahn, S. H. Size-Dependent Work Function and Catalytic Performance of Gold Nanoparticles Decorated Graphene Oxide Sheets. *Applied Catalysis A: General* **2014,** *469*, 159-164.
(49) Ding, Z.; Hao, Z.; Meng, B.; Xie, Z.; Liu, J.; Dai, L. Few-Layered Graphene Quantum Dots as Efficient Hole-Extraction Layer for High-Performance Polymer Solar Cells. *Nano Energy* **2015,** *15*, 186-192.
(50) Jin, S. H.; Kim, D. H.; Jun, G. H.; Hong, S. H.; Jeon, S. Tuning the Photoluminescence of Graphene Quantum Dots through the Charge Transfer Effect of Functional Groups. *ACS Nano* **2013,** *7*, 1239-1245.
(51) Zhu, X.; Zhang, Z.; Xue, Z.; Huang, C.; Shan, Y.; Liu, C.; Qin, X.; Yang, W.; Chen, X.; Wang, T. Understanding the Selective Detection of Fe3+ Based on Graphene Quantum Dots as Fluorescent Probes: The KSp of a Metal Hydroxide-Assisted Mechanism. *Anal. Chem.* **2017,** *89*, 12054-12058.

(52) Qi, H.; Teng, M.; Liu, M.; Liu, S.; Li, J.; Yu, H.; Teng, C.; Huang, Z.; Liu, H.; Shao, Q. Biomass-Derived Nitrogen-doped Carbon Quantum Dots: Highly Selective Fluorescent Probe For Detecting Fe3+ Ions and Tetracyclines. *J. Colloid Interface Sci.* **2019,** *539*, 332-341.
(53) Ju, J.; Chen, W. Synthesis of Highly Fluorescent Nitrogen-doped Graphene Quantum Dots for Sensitive, Label-Free Detection of Fe (III) in Aqueous Media. *Biosens. Bioelectron.* **2014,** *58*, 219-225.
(54) Li, Z.; Ye, R.; Feng, R.; Kang, Y.; Zhu, X.; Tour, J. M.; Fang, Z. Graphene Quantum Dots Doping of Mos2 Monolayers. *Advanced Materials* **2015,** *27*, 5235-5240.
(55) Ganguly, M.; Mondal, C.; Pal, J.; Pal, A.; Negishi, Y.; Pal, T. Fluorescent Au(I)@Ag2/Ag3 Giant Cluster for Selective Sensing of Mercury (II) Ion. *Dalton Trans.* **2014,** *43*, 11557-11565.
(56) Haider, G.; Roy, P.; Chiang, C. W.; Tan, W. C.; Liou, Y. R.; Chang, H. T.; Liang, C. T.; Shih, W. H.; Chen, Y. F. Electrical‐Polarization‐Induced Ultrahigh Responsivity Photodetectors Based on Graphene and Graphene Quantum Dots. *Adv. Funct. Mater.* **2016,** *26*, 620-628.
(57) Ghosh, J.; Ghosh, R.; Giri, P. K. Strong Cathodoluminescence and Fast Photoresponse from Embedded CH3NH3PbBr3 Nanoparticles Exhibiting High Ambient-Stability. *ACS Appl. Mater. Interfaces* **2019,** 11, 14917-14931 .
(58) Yen, Y.-C.; Chen, J.-A.; Ou, S.; Chen, Y.-S.; Lin, K.-J. Plasmon-Enhanced Photocurrent Using Gold Nanoparticles on a Three-Dimensional Tio2 Nanowire-web Electrode. *Sci. Rep.* **2017,** *7*, 42524-42532.
(59) Bampoulis, P.; Sotthewes, K.; Siekman, M. H.; Zandvliet, H. J. Local Conduction in Mo x W1–x Se2: The Role of Stacking Faults, Defects, and Alloying. *ACS Appl. Mater. Interfaces* **2018,** *10*, 13218-13225.
(60) Paul, K. K.; Mawlong, L. P.; Giri, P. K. Trion-Inhibited Strong Excitonic Emission and Broadband Giant Photoresponsivity from Chemical Vapor-Deposited Monolayer MoS2 Grown in Situ on TiO2 Nanostructure. *ACS Appl. Mater. Interfaces* **2018,** *10*, 42812-42825.
(61) Dhar, S.; Majumder, T.; Mondal, S. P. Graphene Quantum Dot-Sensitized Zno Nanorod/Polymer Schottky Junction UV Detector with Superior External Quantum Efficiency, Detectivity, and Responsivity. *ACS Appl. Mater. Interfaces* **2016,** *8*, 31822-31831.
(62) Dutta Chowdhury, A.; Doong, R.-a. Highly Sensitive and Selective Detection of Nanomolar Ferric Ions using Dopamine Functionalized Graphene Quantum Dots. *ACS Appl. Mater. Interfaces* **2016,** *8*, 21002-21010.

Tables:

Table 1: Comparison of the atomic concentration (%) of C, N, O, Au in N-GQDs and Au@N-GQDs, as revealed from the XPS analysis.

Characteristic peaks	N-GQDs	Au@N-GQDs
C 1s	54%	66.8%
N 1s	10%	5.2%
O 1s	36%	27.5%
Au 4f	-	0.5%

Table 2: Comparison of performance of GQD based sensors for Fe^{3+} sensing reported in the literature and the present work.

Sensing Platform	Detection Range (nM)	Limit of detection (nM)	Reference
N-GQDs	3,320 - 32,260	746.2	[52]
N-GQDs	1000 - 19,45,000	90.0	[53]
N-GQDs	1000 - 70,000	80.0	[10]
Dopamine-GQDs	20 - 2,000	7.6	[62]
S,N-GQDs	12 - 1,000	1.7	[8]
Au@N-GQDs	1 - 10,000	1.0	*This Work*

Table 3: Comparison of the performance of GQDs based photodetectors reported in the literature and the present work.

Sample/ Device structure	Operating Voltage(V)	Responsivity (A/W)	Detectivity ($cm \cdot Hz^{1/2}/W$)	EQE (%)	Rise/fall time	Ref.
GQDs	5	0.002	9.59×10^{11}	5.9	64 ms / 43 ms	[18]
Graphene/GQDs/ graphene	5.5	0.5	2.4×10^{11}	80	- / 30 μs	[24]
N-GQD	5	0.103	1.5×10^{10}	24.4	302 ms / 208 ms	*This work*
Au@N-GQD	5	1.36	2.03×10^{11}	292.2	23 μs /100 μs	*This work*

Figures:

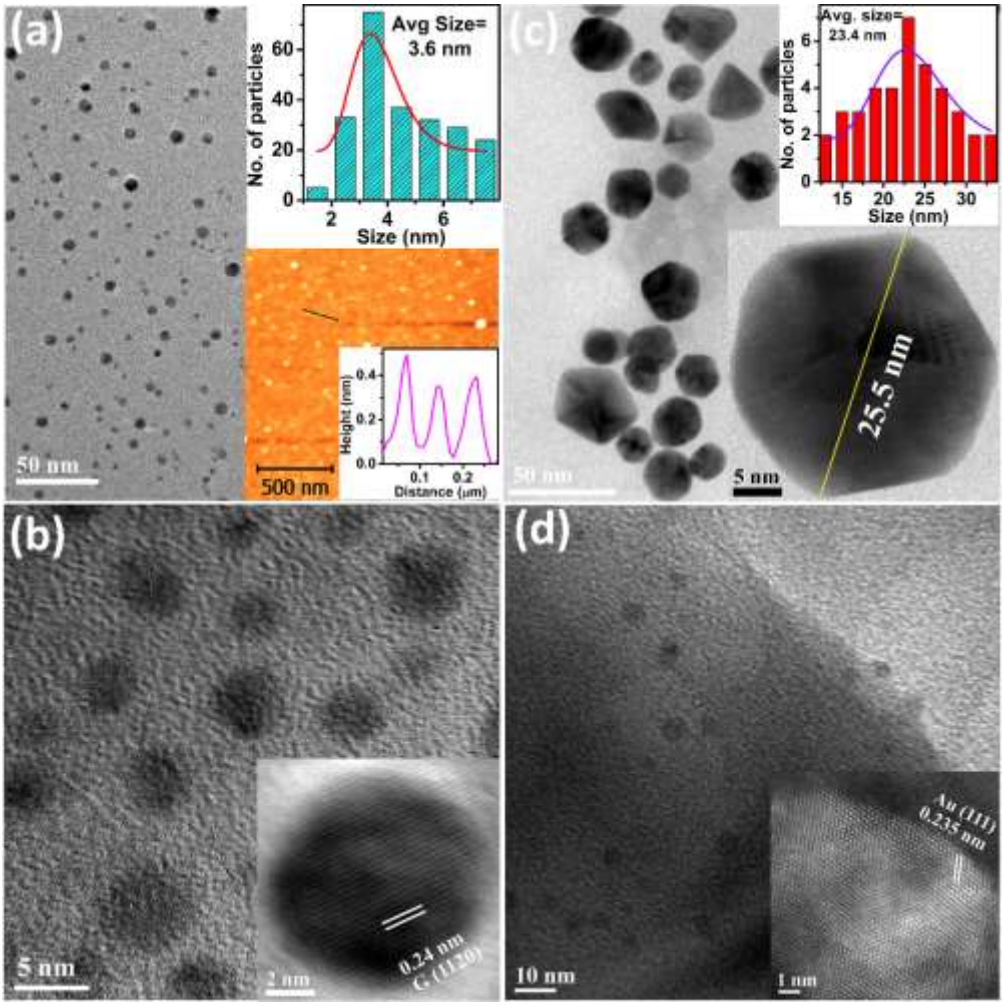

Figure 1: (a) TEM image of N-GQDs; the corresponding size distribution with log-normal fitting is shown in the upper right inset. AFM image of N-GQDs with the height profile is presented in the lower right inset. (b) The HRTEM image of a N-GQDs. The inset shows a single N-GQD with lattice spacing 0.24 nm corresponding to (1120) hcp plane. (c) The TEM image of as-synthesized Au@N-GQDs with a mostly hexagonal shape and some with pentagonal, triangular, and spherical shapes. The upper right inset shows the particle size distribution and the corresponding lognormal fitting. A hexagonal-shaped Au NP with size ~ 25.5 nm is shown in the magnified scale in the lower right inset. (d) The HRTEM image of the Au@N-GQD showing the decoration of N-GQDs on an Au NP. The inset shows the HRTEM lattice fringes of an Au NP.

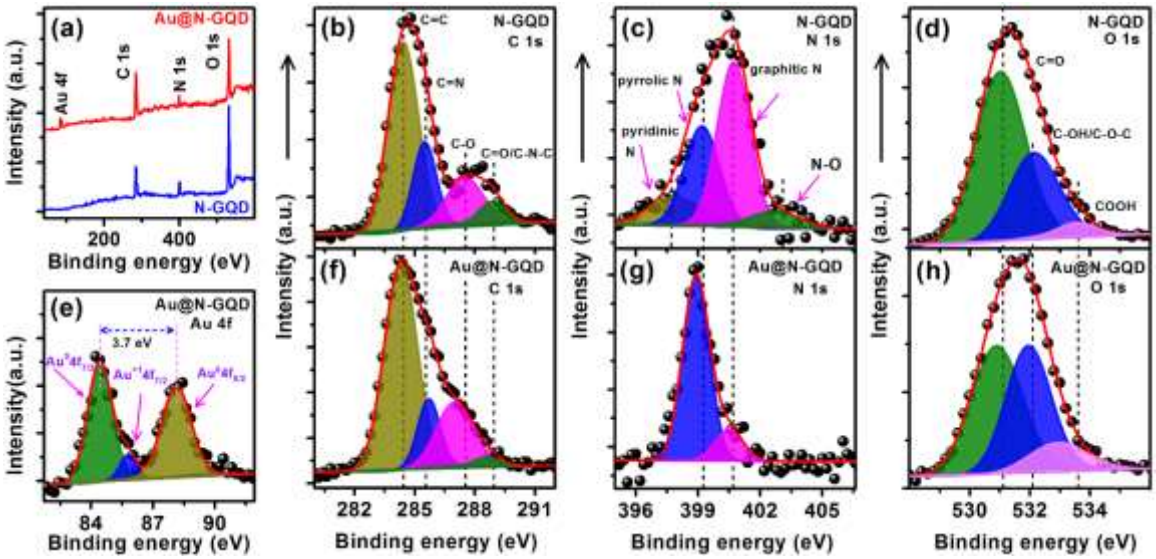

Figure 2: (a) XPS survey scan spectra of N-GQDs and Au@N-GQDs. (b-d) High-resolution XPS spectra of C1s, N 1s, and O 1s, respectively, of N-GQDs. (e-h) Au 4f, C1s, N 1s and O 1s XPS spectra of Au@N-GQDs, respectively. Each spectrum is fitted with a Shirley baseline. The symbols represent the experimental data, and the filled areas correspond to the Gaussian fits of different energy states.

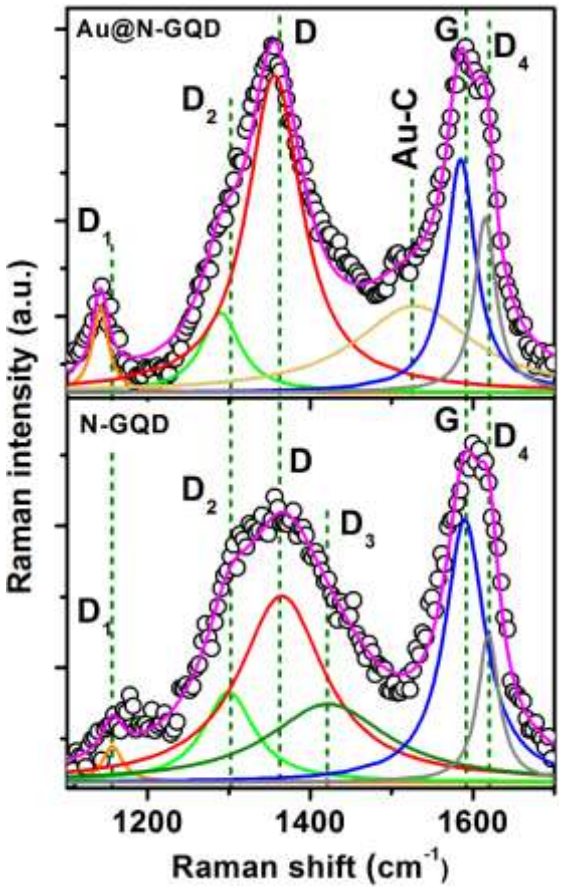

Figure 3: A comparison of the deconvoluted Raman spectra of as-synthesized N-GQDs and Au@N-GQDs. The symbol indicates the experimental data and the solid lines represent the fitted curves. The deconvoluted Raman peaks are labeled as D_1, D_2, D, D_3, G and D_4, and the respective peak positions are indicated with vertical dashed lines.

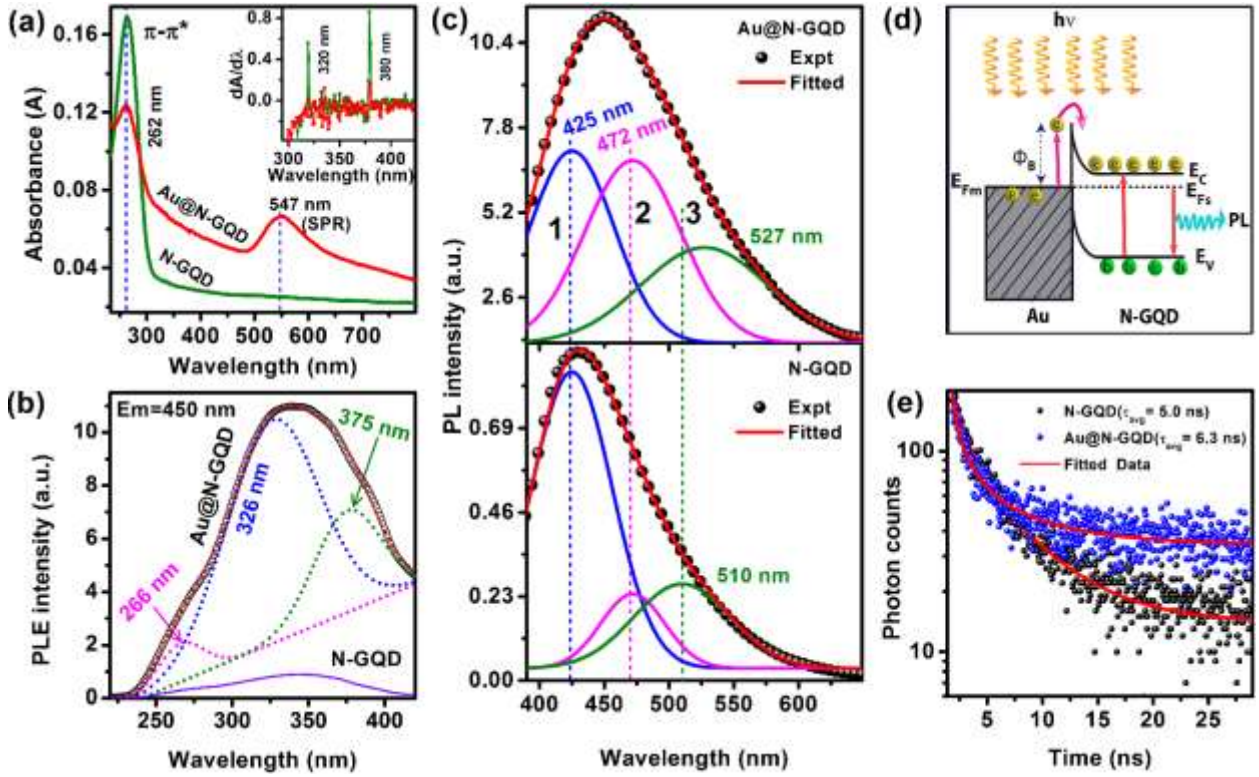

Figure 4: (a) Comparison of the UV-Vis absorption spectra of N-GQDs and Au@N-GQDs. The vertical dashed lines show the absorption peaks corresponding to N-GQDs (262 nm) and plasmonics Au NPs (547 nm). The inset shows the differentiated spectra i.e., the variation of dA/dλ with wavelength (λ) exhibiting two peaks at 320 nm and 380 nm. (b) The PLE spectra of N-GQDs and Au@N-GQDs monitored at the emission position 432 nm and 450 nm, respectively. The PLE spectra of Au@N-GQDs is deconvoluted with three Gaussian peaks. The dashed curves represent the fitted peaks, and the symbol corresponds to the experimental data of Au@N-GQDs. (c) A comparison of the deconvoluted PL spectra of N-GQDs and Au@N-GQDs. (d) Schematic illustration of the band diagram and the electron transfer in Au@N-GQDs under light irradiation giving rise to enhanced PL intensity. (e) Comparison of the TRPL spectra of N-GQDs and Au@N-GQDs.

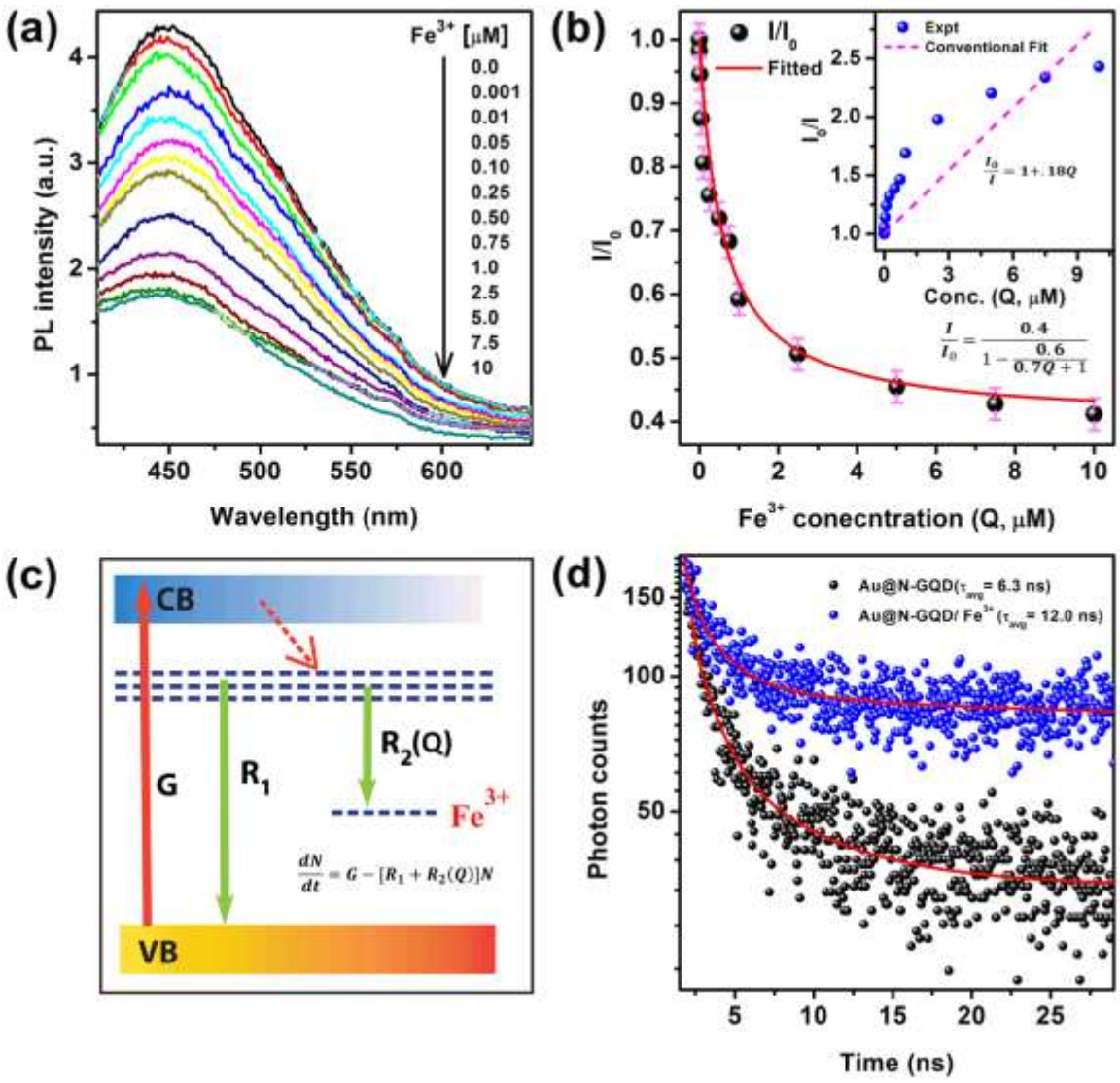

Figure 5: (a) The PL spectra of Au@N-GQDs before and after the addition of Fe^{3+} (0.001-10 μM) with the excitation of 350 nm. (b) The relative change in PL intensity (I/I_0) as a function of Fe^{3+} concentration. The inset shows the variation of I_0/I vs. Q, which strongly deviates from the conventional Stern-Volmer plot (dashed line). (c) The energy band diagram showing the generation (G), recombination (R_1, R_2) pathways for carriers in the presence of Fe^{3+}. The horizontal dashed lines represent the defect levels in Au@N-GQDs. (d) TRPL decay spectra of Au@N-GQDs before and after the addition of Fe^{3+} monitored at 450 nm with 375 nm laser excitation.

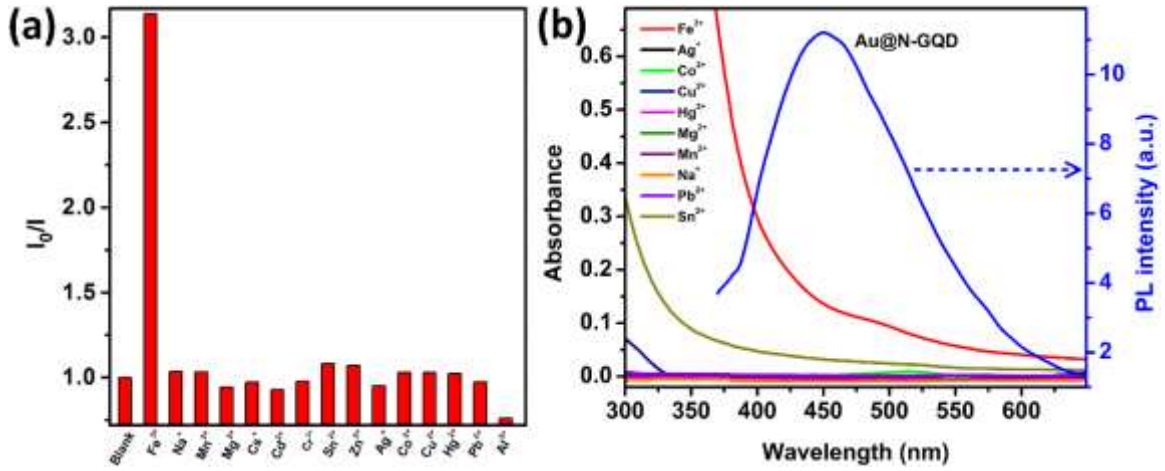

Figure 6: (a) Selectivity of Au@N-GQDs for Fe^{3+} sensing measured by fluorescence quenching (I_0/I) of Au@N-GQDs with the presence of 10 μM concentration of different metal ions. (b) A comparison of the absorption spectra of various metal ions and the spectral overlap of the emission spectra of Au@N-GQDs with the absorption spectra of Fe^{3+} ions.

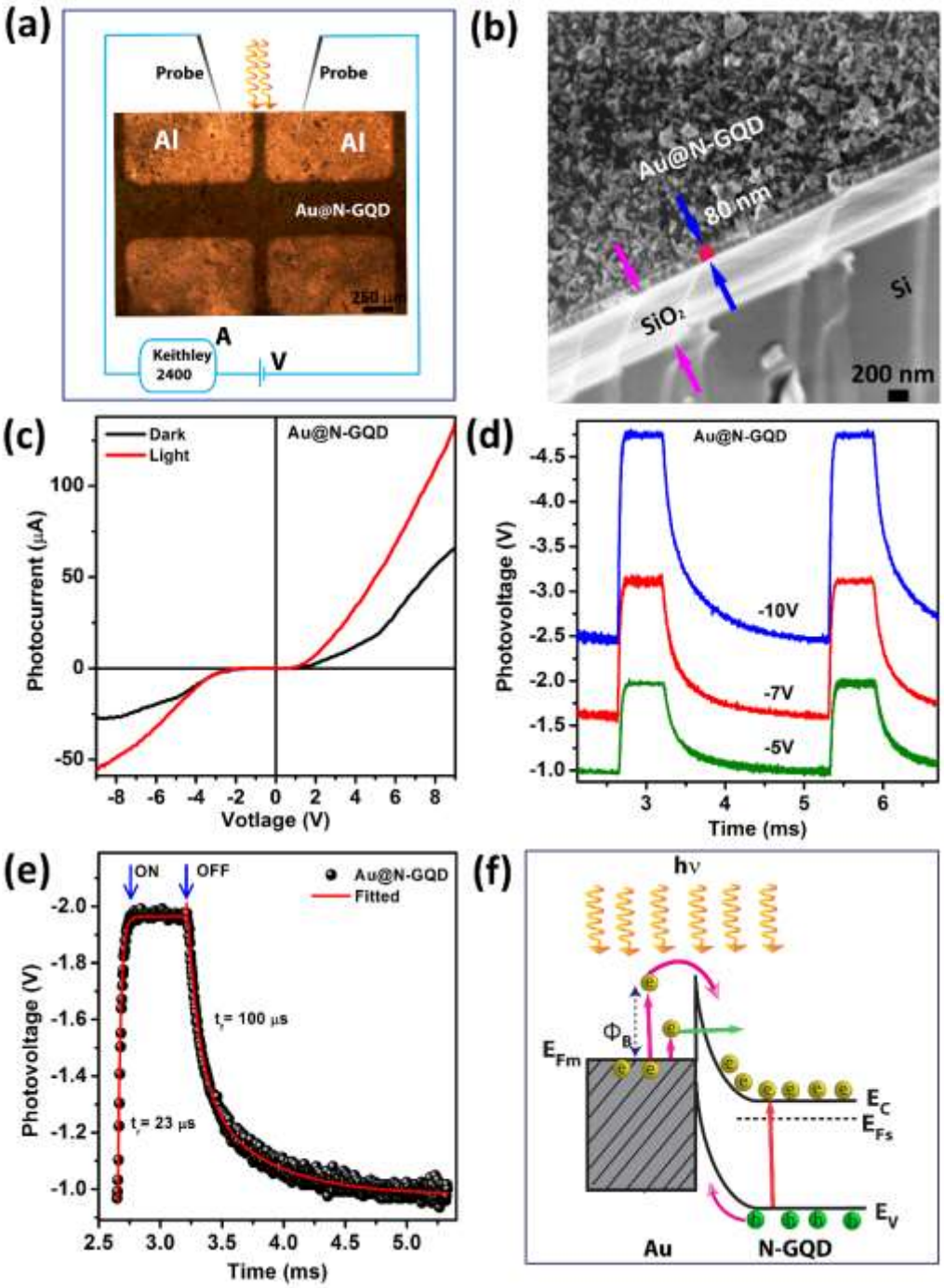

Figure 7: (a) Schematic illustration of the photodetector measurement, with an optical image of patterned Al electrodes on top of the Au@N-GQDs film. (b) Cross-sectional FESEM image of uniform Au@N-GQDs film on SiO_2/Si substrate. (c) The typical I-V characteristic of the Au@N-GQDs layer measured under the dark and light (405 nm laser with power 3.68 mW/cm^2). (d) Temporal response of the photodetector with different bias (-5 V to -10 V). (e) Single magnified photoresponse curve with 405 nm pulsed laser for estimating rise/fall times of Au@N-GQD photodetector. (f) Schematic of the band diagram of Au@N-GQDs with illumination under reverse bias (V<0).

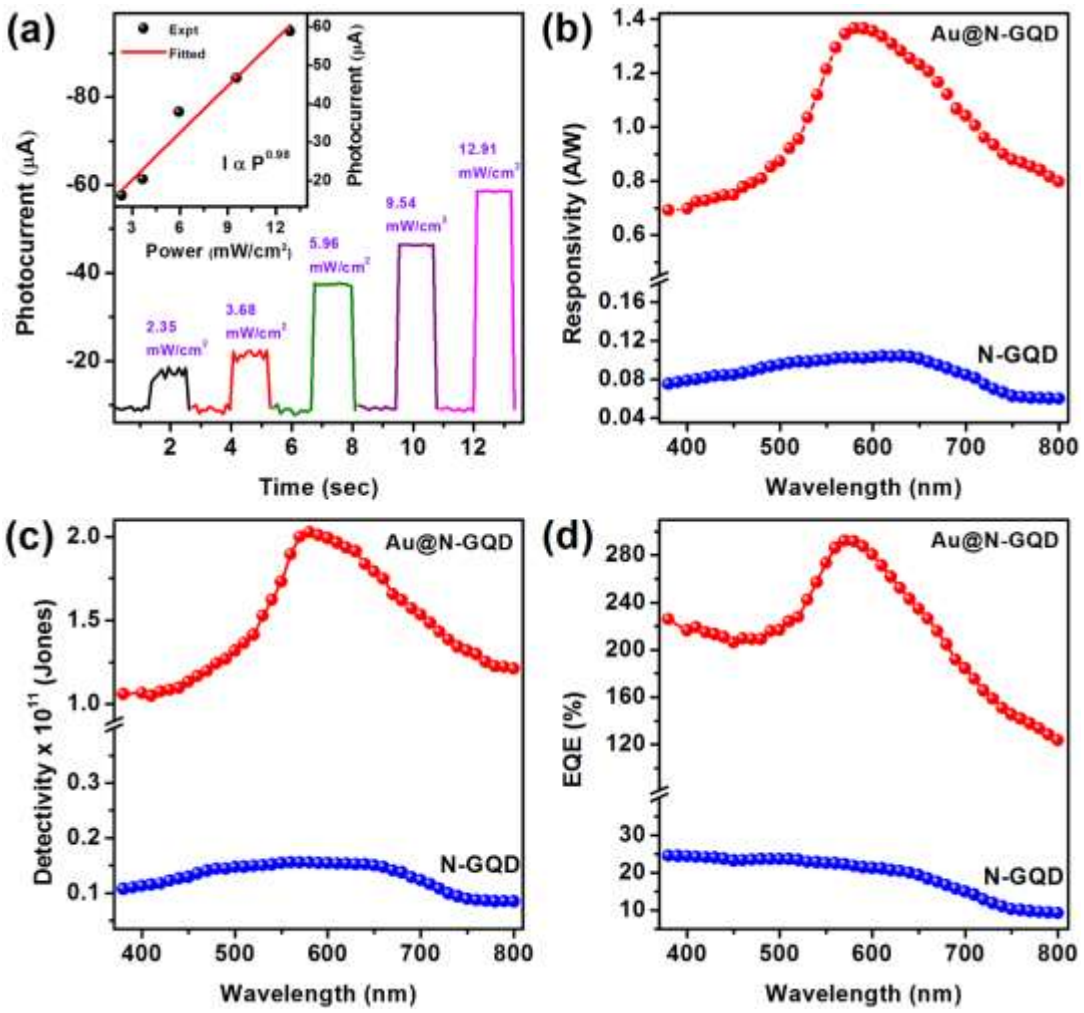

Figure 8: (a) Excitation power-dependent temporal response of photocurrent in Au@N-GQDs with 405 nm pulsed laser excitation. The inset shows the corresponding dynamic response of the photodetector. A comparison of (b) responsivity, (c) detectivity, and (d) EQE of N-GQDs and Au@N-GQDs under 5 V bias.

Graphical Abstract: